Elsevier Editorial System(tm) for Materials and Design

Manuscript Draft

Manuscript Number: JMAD-D-17-06541R2

Title: Fatigue assessment of multilayer coatings using lock-in thermography

Article Type: Research Paper

Keywords: Fatigue; Multilayer; Coating; Infrared Thermography; Bearing; Sn-Ni-Cu systems

Corresponding Author: Mr. Andreu Laborda,

Corresponding Author's Institution: University of Southampton

First Author: Andreu Laborda

Order of Authors: Andreu Laborda; Andrew Robinson; Shuncai Wang; Yi Zhang; Philippa Reed

Abstract: Plain bearings experience cyclic loading during operation, which may cause fatigue failure. In the bearings under study a steel backing has a leaded bronze interlayer, covered by a thin (20 □m) multilayer coating, which consists of several electroplated layers composed of Sn, Ni and Cu. Commercial performance assessments simulate the conditions of engines in a 'Pass or Fail' test. A new methodology is proposed to assess the fundamental fatigue behaviour for such complex layered bearings. Accelerated fatigue tests on half-shell bearings have been conducted under 3-point bend, whilst the coated side of the bearings are recorded with an infrared camera. Cyclic tests with strain gauges placed on the coating have been performed to evaluate the strains developing during loading. By combining these tests we can rank different coatings. A compliance based failure criterion is also compared with a failure criterion based on early damage revealed by infrared thermography, showing that the latter is far less conservative. Thus, this methodology allows detection of small scale fatigue cracks in the coatings significantly earlier, facilitating assessment and identification of possible mechanisms to explain the differences in fatigue performance between coatings. This provides valuable information to develop new coatings for future bearing designs.

Detailed Response to Reviewers

Dear Prof Marco Sebastiani,

We were pleased to find that the editor and the reviewers felt our paper was publishable, subject to a few further corrections, and we believe we have now responded to all these comments made by reviewers and the editor. We have addressed each comment below (and highlighted the associated changes in the revised manuscript in yellow). We trust the final corrected paper will now be found to be publishable in Materials and Design.

Reviewer #3:

"1, The reputable profiles of elements are still present in Fig.4."

Response: We have now removed the elemental profiles from the SEM pictures of Fig.4.

"2, As shown in Fig.12, one can not observe the grain size and grain boundaries from the optical microscopy image and the authors have to provide the clear images to show the detail information about grains which related to the propagation of fatigue crack."

Response: We appreciate this is a good point and we are planning to perform extensive EBSD mappings to obtain grain size information, however, the current paper aims to report primarily a new methodology developed to test coatings and as part of this to simply introduce some of the possible competing micromechanisms that control fatigue behaviour. Therefore, although the paper discusses the possible effects of relative grain sizes between coatings, at this stage it is only based on (referenced) assumptions about grain size based on the manufacturing process. This is an ongoing research project and future publications are planned (and explicitly mentioned within the paper) which will focus in far more detail on the microstructure and how it affects fatigue performance. In addition if we were to add the suggested considerable additional characterisation detail we will significantly extend the paper beyond the recommended journal paper length.

"3, The reviewer believe the explanation for the propagation of the fatigue crack in the three kinds of architecture samples, as discussed at 3.4,is ambiguous and unreadable. So, it have to be further improved."

Response: In order to make Section 3.4 more readable we have now divided this into three sub-sections: Thermographic observations, Surface observations and Cross-sectional observations. This should now make clearer the difference between discussion of the surface cracks and the cross-sectional cracks (which the reviewer mentioned previously) and we have also re-written the paragraphs related to intergranular crack propagation in Sn in order to make this less ambiguous. The authors believe that with this restructuring the paper reads much better and thank Reviewer#3 for the input.

"4, The reviewer still believe the conclusion of this manuscript should be shorter."

Response: We have now made the conclusions 25% shorter and note that at ~450 words this is commensurate with typical length of conclusions for similar length papers previously published in Materials and Design.

*Graphical Abstract

Click here to download high resolution image

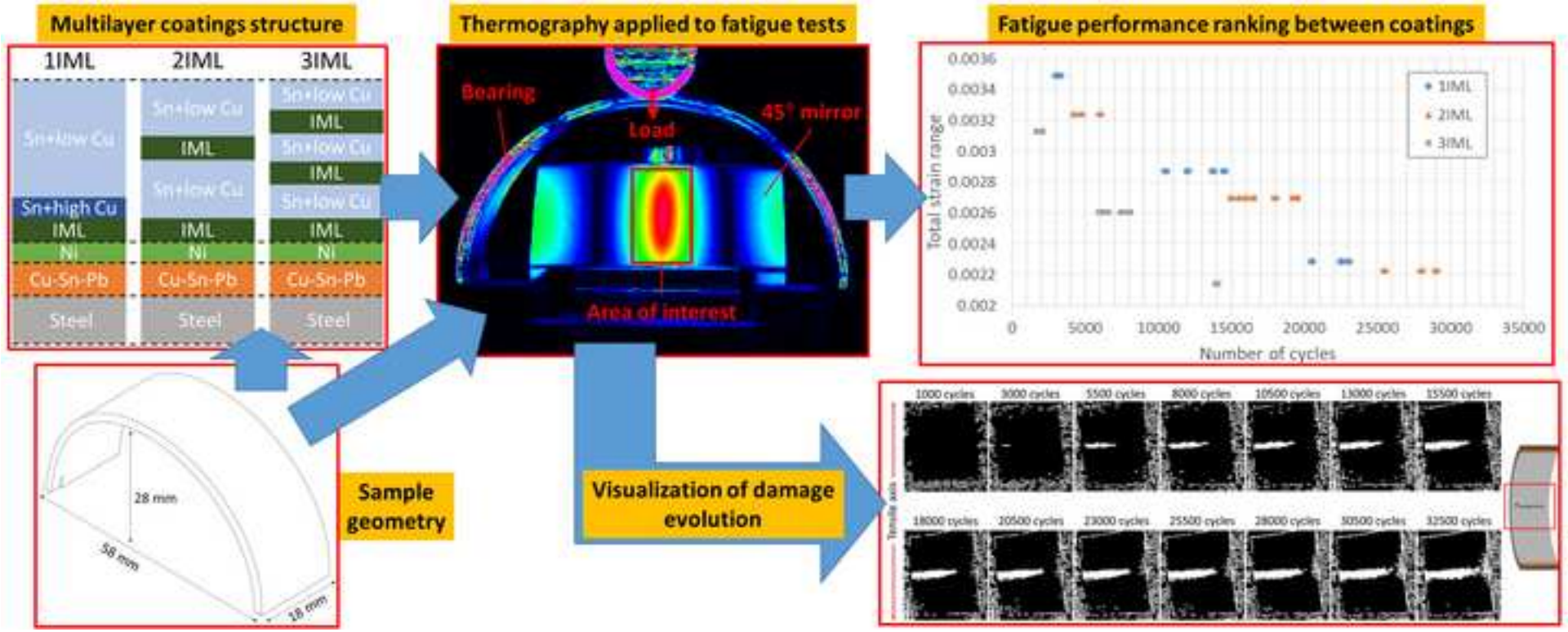

Highlights

- The use of Infrared Thermography allows ranking of the fatigue performance of different multilayer coatings during fatigue tests.
- The new methodology detects damage earlier than previous methodologies, enabling the use of a failure criterion which is far less conservative.
- The multilayer coating with two intermetallic layers (IML) shows better fatigue performance than the coatings with one and three IML.

Fatigue assessment of multilayer coatings using lock-in thermography

Andreu Laborda[1]*, Andrew Robinson[1], Shuncai Wang[2], Yi Zhang[3], Philippa Reed[1]

[1]Engineering Materials Group, Faculty of Engineering and Environment, University of Southampton, UK
[2]nCATS, Faculty of Engineering and the Environment, University of Southampton, Southampton, UK
[3]Daido Metal Co. Ltd, European Technical Centre (UK), Winterhay Lane, Ilminister, TA19 9PH, UK

*A.Laborda@soton.ac.uk; Building 5, Highfield Campus, Southampton SO17 1BJ, United Kingdom.

Highlights

- The use of Infrared Thermography allows ranking of the fatigue performance of different multilayer coatings during fatigue tests.
- The new methodology detects damage earlier than previous methodologies, enabling the use of a failure criterion which is far less conservative.
- The multilayer coating with two intermetallic layers (IML) shows better fatigue performance than the coatings with one and three IML.

Abstract

Plain bearings experience cyclic loading during operation, which may cause fatigue failure. In the bearings under study a steel backing has a leaded bronze interlayer, covered by a thin (20 μm) multilayer coating, which consists of several electroplated layers composed of Sn, Ni and Cu. Commercial performance assessments simulate the conditions of engines in a 'Pass or Fail' test. A new methodology is proposed to assess the fundamental fatigue behaviour for such complex layered bearings. Accelerated fatigue tests on half-shell bearings have been conducted under 3-point bend, whilst the coated side of the bearings are recorded with an infrared camera. Cyclic tests with strain gauges placed on the coating have been performed to evaluate the strains developing during loading. By combining these tests we can rank different coatings. A compliance based failure criterion is also compared with a failure criterion based on early damage revealed by infrared thermography, showing that the latter is far less conservative. Thus, this methodology allows detection of small scale fatigue cracks in the coatings significantly earlier, facilitating assessment and identification of possible mechanisms to explain the differences in fatigue performance between coatings. This provides valuable information to develop new coatings for future bearing designs.

Keywords

Fatigue; Multilayer; Coating; Infrared Thermography; Bearing; Sn-Ni-Cu systems

Graphical abstract

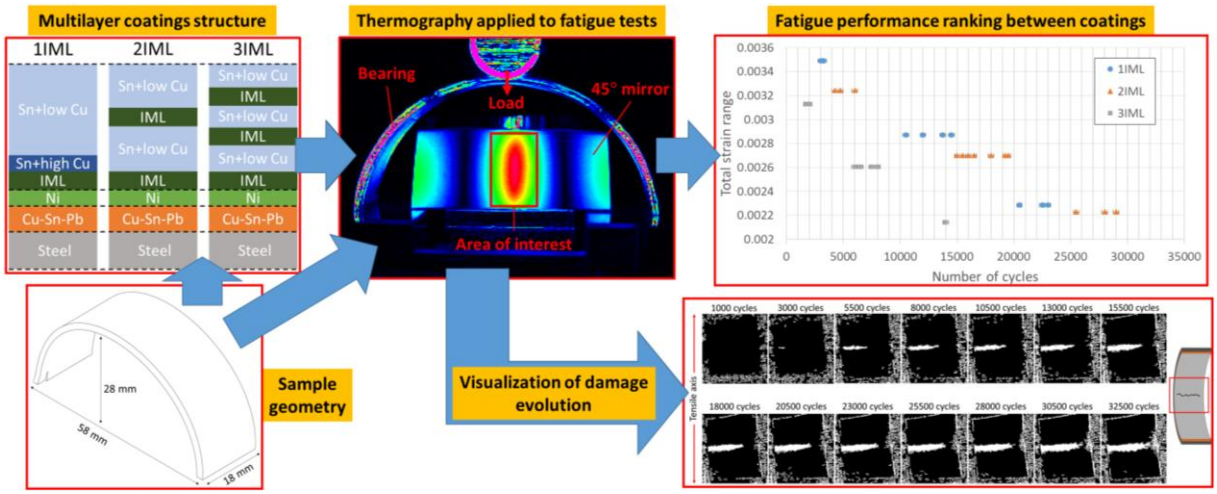

1. Introduction

Plain bearings are a crucial part of internal combustion engines; typically comprising two half-shell bearings fitted together into a housing, supporting the crankshaft or the connecting rod. Multilayer coatings are used in such devices in order to reach a property compromise or balance between hard and soft materials, since a bearing needs to have high mechanical strength but also has to be able to embed foreign particles that could damage the crankshaft. The material system considered in this work comprises multilayer coatings made of Sn-Ni-Cu electrodeposited onto a leaded bronze interlayer bonded to a steel-backing (Figure 1). In service, the engine loads are transferred to the bearing coating through a thin oil film, hydrodynamic pressure concentration variations of such oil films lead to dynamic stress fields, applying cyclic loading, which may then lead to cracking and spalling of these coatings [1].

Engine manufacturers are always trying to increase the power output, while decreasing the weight and size of new engines, thus increasing the loads that the plain bearings have to support. In response, coating architectures for bearings have become more and more complex in order to increase the fatigue lifetime under higher service loads. Such coating systems now comprise overlay bearings that consist of complex micrometre scale-multilayer structures (1-18 μm per layer) [2, 3], that make the fatigue assessment process more complex, in particular detecting early damage in the coatings is challenging [4, 5]. Previous methods have been based on detecting a compliance change in far thicker coatings.

In industry, accelerated test rigs are used to rank the fatigue performance of bearings by testing them to failure in an engine-like environment. One example is the Sapphire test machine [6], which simulates service loading by rotating an eccentric test shaft within the test bearing, where the dynamic load is applied as the result of oil film pressure between the bearing and the shaft due to the motion of the shaft. This is a useful pass-fail test to rank bearings in an engine-like environment; however, it does not offer insight into the fatigue mechanisms controlling the performance. Without a mechanistic understanding of what controls the fatigue performance of these layered systems, optimisation of bearing layer architectures and the microstructures of the various coatings is “black box” and can only be achieved empirically through trial and error.

In previous studies, simple bending tests have been used to test fatigue performance of coated systems [7-9]. This approach has also been adapted to test half-shell bearings, using a 3-point-bend

configuration, in order to assess their fundamental fatigue performance. Several researchers have used such methodologies to assess relatively thick (400-180 μm) bilayer aluminium based coatings in plain journal bearings: *M.C. Mwanza et al.* [10] studied the different fatigue performance of aluminium based bilayer bearings with different lining compositions, *Ali et al.* [11] compared the fatigue performance of bearings produced by different manufacturing processes (HVOF versus roll bonding), and *Joyce et al.* [12] investigated the effect of environment by testing Al-Sn-Si bearing linings under oil, vacuum and air conditions. Each of these test methodologies involve simpler loading cases than the Sapphire rig, and hence allow the effect of changing the load levels, frequency, environment, etc, to be investigated. In addition, since the test configuration is simple, access to the lining surface of the sample is relatively easy, which allows monitoring techniques, such as strain gauging or different kinds of imaging (including replica approaches combined with optical microscopy) [13-20] to investigate the test in-situ during testing. A substantial increase in fatigue evolution observations becomes possible (e.g. crack initiation and growth) that helps us to understand what happens during the test. The simpler loading case also allows better control of the test conditions and the ability to link the effect of these more directly to the observed fatigue mechanisms.

The application of infrared thermography as a full-field, non-contact, non-destructive method to detect damage has been increasingly studied in the past years. Infra-red thermography has been successfully used for several applications related to damage detection such as monitoring civil structures [21-23], exploring plastic deformations [24] and evaluation of fatigue damage in materials [25-29]. For instance, *Ummenhofer et al.* [30] applied thermographic approaches to investigate localized damage occurring due to fatigue on welded structures during tests, showing the great potential of such techniques in detecting and studying the evolution of localized damage throughout lifetime.

Moreover, lock-in infrared thermography allows investigation of the temperature distribution on the surface of a cyclically loaded component by using the loading signal to filter out all temperature measurement that is not fluctuating and the same frequency as the test. This enables erroneous temperature changes to be disregarded, reduces significantly the measurement noise and allows for the detection of even smaller changes in temperature that are only related to the applied fatigue loading. Researchers have used this variant to successfully evaluate fatigue parameters and also evaluate the occurrence of fatigue damage in metals [25, 31, 32]. In this study we have introduced this observation approach to particularly investigate the fatigue performance of multilayer overlay bearing coatings and the detection of cracks.

The present work proposes a significant improvement to established fatigue evaluation methodologies [10-12] by using lock-in thermography approaches. This will enable the assessment of fatigue performance of thin coatings (where replication approaches are less successful in tracking fatigue initiation and growth processes on the very thin electroplated coatings), and the improvement of damage assessment location in post-mortem observations. Such improvements help elucidate the mechanisms leading to the fatigue and fracture of the coatings [33, 34], making possible the optimization and informed design of new fatigue resistant bearings. This is in contrast to the empirical process followed by using industry standard approaches such as the Sapphire test. This methodology also offers opportunities to detect early damage in other coated structures and geometries, showing its wider applicability beyond the bearing domain.

2. Materials and Methods

2.1 *Specimens*

The specimens tested are standard semi-circular bearings (Figure 1a), consisting of a steel backing, a leaded bronze interlayer and the final multilayer coatings. Such coatings have thin nickel based and tin based layers applied to the bronze interlayer by proprietary electroplating approaches. Preceding the electroplating coating procedure, the substrate was degreased with an alkaline cleaner and etched in a solution of diluted hydrochloric acid. Finally, the coating is electroplated: the tin based layers are electroplated from an electrolyte containing acid, tin ion, copper ion and a proprietary additive package; and the nickel based layers are produced from a Watt's bath. Once coated, the specimens are thermally annealed in order to create nickel-tin intermetallic compound layers and also to stabilize the microstructure for service conditions [3, 35].

Three types of multilayer coatings were investigated (Figure 1b): the first coated system consists of a nickel diffusion barrier between the leaded bronze interlayer and the subsequent intermetallic layer, then the deposition of a fine Sn based layer with 10%wt. of Cu (Sn+high Cu) and a final top Sn layer with 3%wt. of Cu (Sn+low Cu). The second coated system on top of the bronze interlayer, comprises firstly a nickel barrier layer, then an intermetallic layer, a Sn-Cu (3%wt.) layer, a second intermetallic layer and then a further Sn-Cu (3%wt.) layer. Similarly, the third coating system emulates the second one but contains an additional third intermetallic layer and a Sn-Cu (3%wt.) layer on the top. These coatings are designated as 1IML, 2IML and 3IML, referring to the number of intermetallic layers: 1, 2 and 3 intermetallic layers, respectively.

In order to study the fatigue performance of the coatings, the rest of the bearing structure was maintained the same for all the specimens. The steel backing and leaded bronze interlayer had the same thickness and composition for all the samples, only the top multilayer coating configuration changed among the three types of specimens.

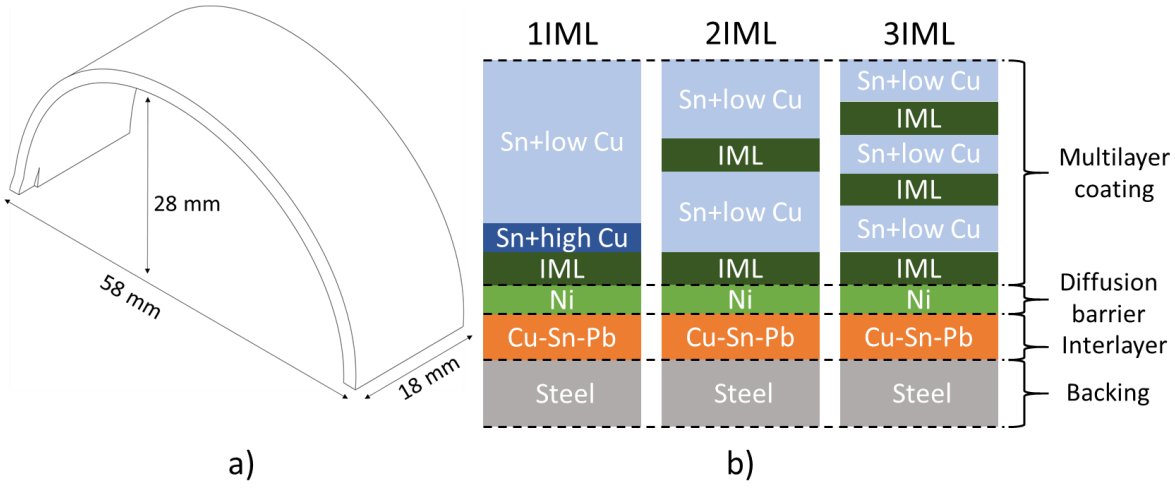

Figure 1. Schematics of: a) a bearing and b) cross-sectional structures of the specimens (not to scale).

2.2 *Sample preparation*

To allow the use of thermography, the coated side of the specimens is painted with matt black paint in order to provide a uniform and high surface emissivity and to make the specimens behave as a 'black body', i.e. only emitting heat radiation, hence, avoiding reflections of radiation coming from surrounding bodies [36]. The samples were first submerged in acetone for degreasing and painted

applying ~20 μm of ELECTROLUBE Matt Black Paint, widely used for thermography applications. In order to achieve this paint thickness, each sample was painted in separate passes, waiting 20 minutes between passes to allow the paint to dry. Each pass consisted of a single movement of the spray can across the specimen at approximately 1 m/s with the nozzle positioned at approximately 300 mm from the surface (these values are approximate and are somewhat operator dependent).

2.3 *Fatigue testing*

The specimens were tested in a 3-point bend configuration, with the ends of the bearing constrained in grooves in a steel rig clamped to the test machine base and aligned with the bearing and the load-cell. The load cylinder was aligned with the load-cell and the rig by using an aligner that fits into the rig and allows the correct linear contact between the bearing and the load cylinder in order to ensure test reproducibility. In addition, a Cedip 480M infra-red detector was used to measure temperature changes and conduct lock-in thermography during the fatigue tests. The detector uses an inbuilt 27 mm lens that captures data at rates of 383 Hz for a 320x256 field of view. The noise equivalent temperature difference (NETD) of the infra-red system is 15.56 mK, the lock-in technique allows the NETD to be reduced to approximately 4 mK [37]. A series of 1000 images were recorded every 500 cycles so that changes in the surface temperature due to fatigue could be periodically observed. The camera is aimed at a 45° piece of aluminium with a mirror finish placed below the bearing in order to obtain images from the region of the coating where the maximum stress is developed (Figure 2).

Fatigue tests were carried out on an InstronPuls E1000 electrodynamic test instrument with 1 kN load-cell and digitally controlled by WaveMatrix software. The tests were conducted at 10 Hz and R (load ratio) = 0.1 for different load conditions ranging from 900 N to 500 N maximum load in order to evaluate fatigue behaviour at lifetimes between 10^3-10^5 cycles.

Since the tests were conducted under load control, CEA-06-062UT-120 strain gauges were placed on the area of interest of the coatings i.e. the maximum strain zone, in order to evaluate the strain developed on the top surface of each coating for each set of load conditions.

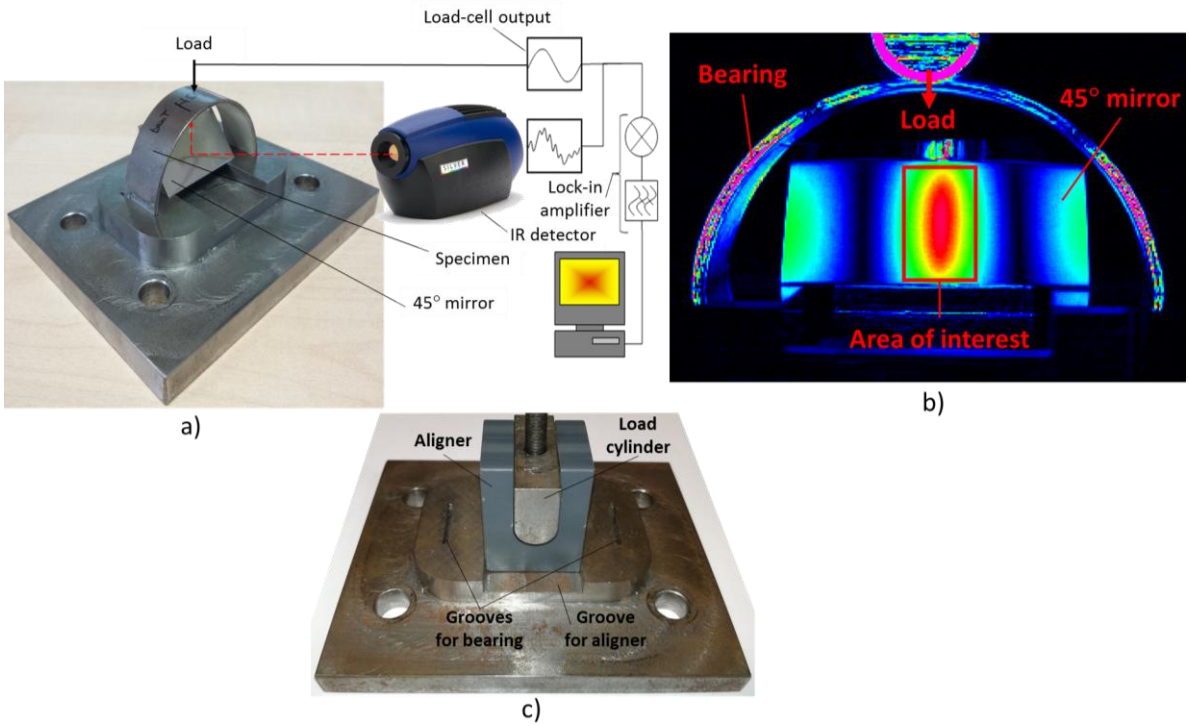

Figure 2. Fatigue test set-up of a 3-point bend configuration with infra-red detector: a) schematic view, b) view of the set-up from the infra-red detector and c) elements used to ensure correct alignment of the bearings.

2.4 *Characterization*

An optical microscope Olympus BX51 was used to observe the presence of cracks on the sample surfaces enabling comparison with the infra-red images obtained. Cross-sections of tested and un-tested bearings were also studied with Scanning Electron Microscopy (SEM). Fine strips of un-tested samples were cut and polished with successively finer grades of silicon-carbide paper (220, 500 and 800), then of diamond suspensions (9, 3 and 1 μm) and finally a colloidal silica suspension (0.06 μm). The multilayer structure of the coating is revealed with a JEOL 6500F Field Emission Gun (FEG)-SEM equipped with an Energy Dispersive X-ray Spectroscopy (EDS) for compositional analysis. Finally, cross-sectional analysis of the fatigue tested samples was conducted using an NVision40 dual system Focussed Ion Beam (FIB)-FEG-SEM, which allows cross-sections of specific locations to be made without damaging sensitive surface features such as cracks.

2.5 *Image processing*

The layer thicknesses of each thin overlay electroplated coating were measured using SEM images at high magnification, and processed to evaluate coating thickness values. Firstly, Fiji-ImageJ is used to select the layer of interest, then to highlight the edges by adjusting the threshold, binarizing the image and then exporting the binarized image to Matlab. Using Matlab, the distance between the two edges for each column of pixels was measured. A similar process was followed to measure the thickness of the interlayer and the backing using optical microscope images.

Using the infra-red camera during the fatigue tests, a certain number of frames or images were recorded and stored sequentially every 500 cycles. The infra-red signal from the camera is correlated to the loading signal from the test machine (known as the lock-in technique), consequently, the level of noise is significantly reduced since only the infra-red response at the specified loading frequency is analysed. The recorded images were processed using AltairLI software, which performs a fast

Fourier transform (FFT) based averaging procedure over all the recorded images to generate three data sets [38]. The first file contains the absolute temperature, T, of the specimen for each pixel. The second file contains the temperature change, ΔT. The third file contains phase data which identifies whether the temperature change was in phase or out of phase with the applied loading. Typically the T and ΔT signals would be used to provide quantitative full field surface stress data via a technique called Thermoelastic Stress Analysis (TSA) which allows temperature change to be directly related to the sum of the principal stresses. Meanwhile the phase signal would be used to identify areas of tensile or compressive stress.

One of the fundamental assumptions of thermoelastic stress analysis is that adiabatic conditions are maintained (i.e. no heating or heat transfer) during the period of time that data is recorded (i.e. from one image to the next). Under adiabatic conditions, an applied stress causing a local volume variation will subsequently cause a local variation in the temperature of that volume, these conditions are achieved where a uniform stress distribution occurs. If non-adiabatic conditions prevail, the measured temperature change will not be as a result of the stress change alone.

Violations in this assumption, i.e. non-adiabatic behaviour, can be readily observed from the phase change information. This assumption can be used to our benefit since the formation and growth of small cracks, and the cyclic plasticity in the region, will cause internal heating (non-adiabaticity) which would manifest itself as a change in phase signal in the region of the damage. Therefore analysis of the phase signal may enable the effect of cracks on the stress field to be detected.

In order to highlight areas with variations in the phase and thereby allowing crack location identification, the images were processed with Matlab using the following steps (Figure 3):

i. Subtract each image from an image of reference, taken at the beginning of each test, in order to obtain the relative change of phase (Figure 3a).
ii. From the resultant image calculate the mean (*m*) and standard deviation (*std*) of the phase-signal in the area of interest in order to quantify the noise within the images (Figure 3b).
iii. Use the results of the previous step as a threshold, in our case we removed the noise with 95% confidence by eliminating all the values below *m+2std* (Figure 3b).
iv. Remove groups of pixels with less than ten members in order to eliminate possible anomalies. Following this process one can obtain images to identify relative changes of phase due to the appearance of cracks in different samples and use them to establish a consistent and quantitative criterion of crack initiation-early crack growth (Figure 3c).

Following this procedure we were able to better identify the fatigue damage detected by the infrared camera.

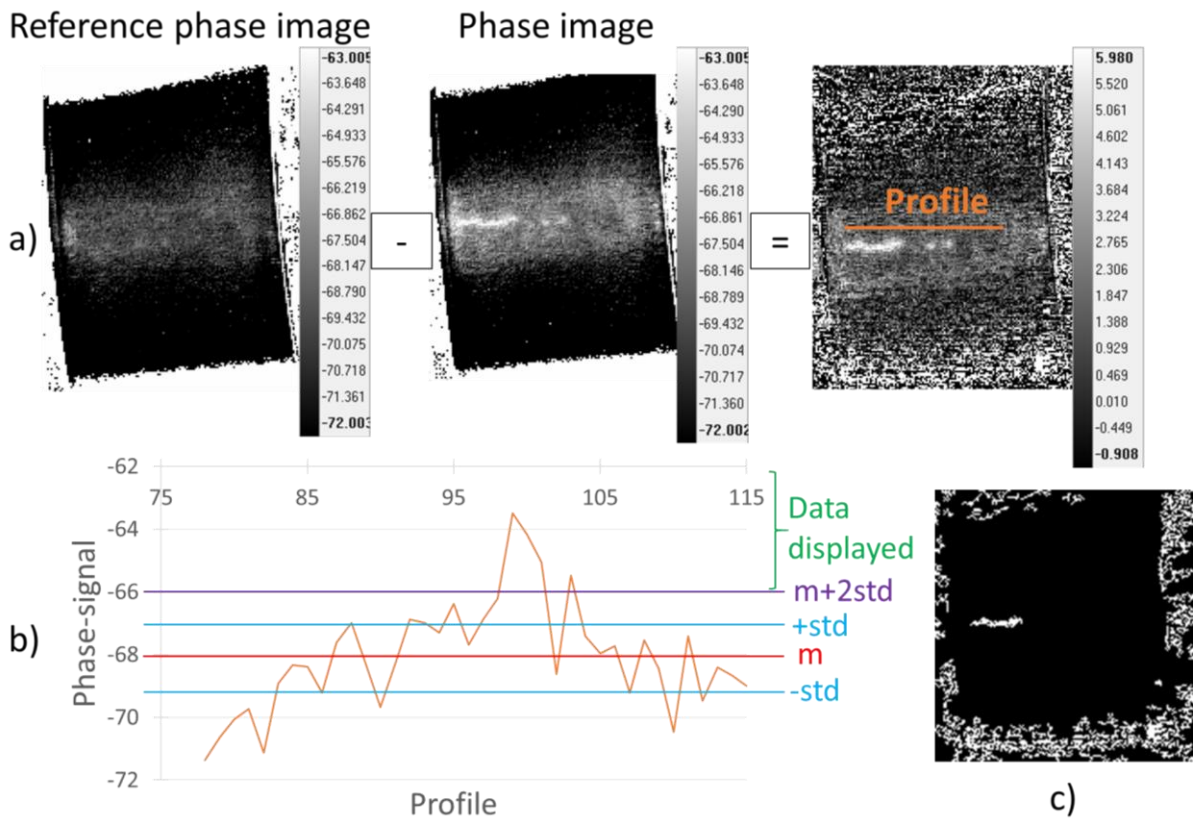

Figure 3. Schematic of the steps followed to process the phase images: a) Subtraction of the image of reference from the image of interest (step i); b) Measurement of the mean (m) and standard deviation (std) of the signal (step ii). Use these results as a threshold by displaying only the data above m+2std (step iii); c) Resultant image, where possible anomalies have been eliminated.

3. Results and Discussion

3.1 Microstructure characterization

The multilayer overlay coating is the only variation between the three bearing architectures, as the same dimensions (and composition) of leaded bronze interlayer and steel backing were used in all the bearings. In order to study the microstructure of the three different overlays, the bearings were therefore cut perpendicular to the coating surface, to assess the cross-sections of the layers.

In Figure 4a one can see an overall cross-section for a 1IML coating. Four distinct, different layers can be seen: at the bottom there is the bronze interlayer (containing lead islands), which will smear out acting as a solid lubricant in case the top coating spalls off or is otherwise removed during service. Above the interlayer the nickel barrier can be seen, then a very thin intermetallic layer and finally the tin top layer with 3%wt. of copper that is believed to provide the best compromise between surface properties and fatigue resistance during service [2]. On being first manufactured, the coating is produced with a Sn layer containing 10%wt. of copper above the nickel layer, and then a Sn-3wt%Cu layer on the top surface, this cannot be distinguished in the SEM after the annealing process. It is believed that this is because most of the copper in the original 10wt% region has diffused to the interface between the Ni and Sn layers (to form the intermetallic), and that this original higher Cu composition profile also acts to reduce the diffusion of Cu from the outermost Sn layers towards the Ni, hence, the system maintains the original properties on the top layer for longer [2].

Similarly, Figure 4b shows the layered structure for the 2IML coating, which also comprises the leaded bronze interlayer and the nickel diffusion barrier that prevents the diffusion of copper up from the interlayer into the subsequent Sn based coatings, thus preventing the formation of Cu_3Sn which is a brittle intermetallic with undesirable properties. Thus the result is that there is a thin intermetallic layer, a Sn based layer, a thicker intermetallic layer of approximately 4 microns and finally the upper ~8 microns is a tin-copper layer with the composition being predominantly tin after thermal annealing. *Y. Zhang et al.* [3] obtained similar results for this structure (2IML), however, they observed some differences in the microstructure for 1IML i.e. the quantity of precipitates in the Sn based layers; this variation is due to the lack of thermal annealing in their structure compared to the coating investigated in this paper.

The structure of the 3IML coating follows the same principle as 2IML combining multiple Ni based and Sn based layers, while utilising two additional layers on the top (Figure 4c). Although the layer thicknesses are reduced proportionally to still achieve 20 micron of total overlay thickness (Table 1).

It can also be observed that after thermal annealing some of the original nickel barrier layer was converted into a tin-nickel intermetallic compound layer, due to the diffusion between Ni and Sn. This also explains why the interface between the Sn-IMC is rougher than the interface between Ni-IMC, since the diffusion between Ni-Sn is faster than Ni-Cu [39, 40].

In all the overlay coatings, it has been observed that the Ni layer is displaced towards (or directly linked to) lead particles when they are close to the Ni barrier layer. This phenomenon can be explained by considering the leaded bronze structure in the top surface plane just before the Ni electrodeposition step. During the electrochemical etching step the lead is preferentially removed creating a difference in the surface level of those materials. Thus the nickel deposited directly above a lead particle would be deposited at a different (lower) level as seen in the cross-sections.

Table 1 outlines the systematic image analysis based thickness evaluations of each layer in the coatings, showing a good agreement with the SEM pictures and EDS analysis in Figure 4.

Table 1. Layer thickness for each coating structure.

	Thickness (mm)		
Layers	**1IML**	**2IML**	**3IML**
Steel backing	1.250	1.250	1.250
Leaded bronze interlayer	0.250	0.250	0.250
Ni diffusion barrier	0.002	0.002	0.002
Bottom IML	less than 0.001	0.001	0.001
Bottom Sn-Cu layer	0.020	0.007	0.006
Middle IML	-	-	0.002
Middle Sn-Cu layer	-	-	0.004
Top IML	-	0.004	0.002
Top Sn-Cu layer	-	0.008	0.005
Total multilayer coating	0.022	0.022	0.022

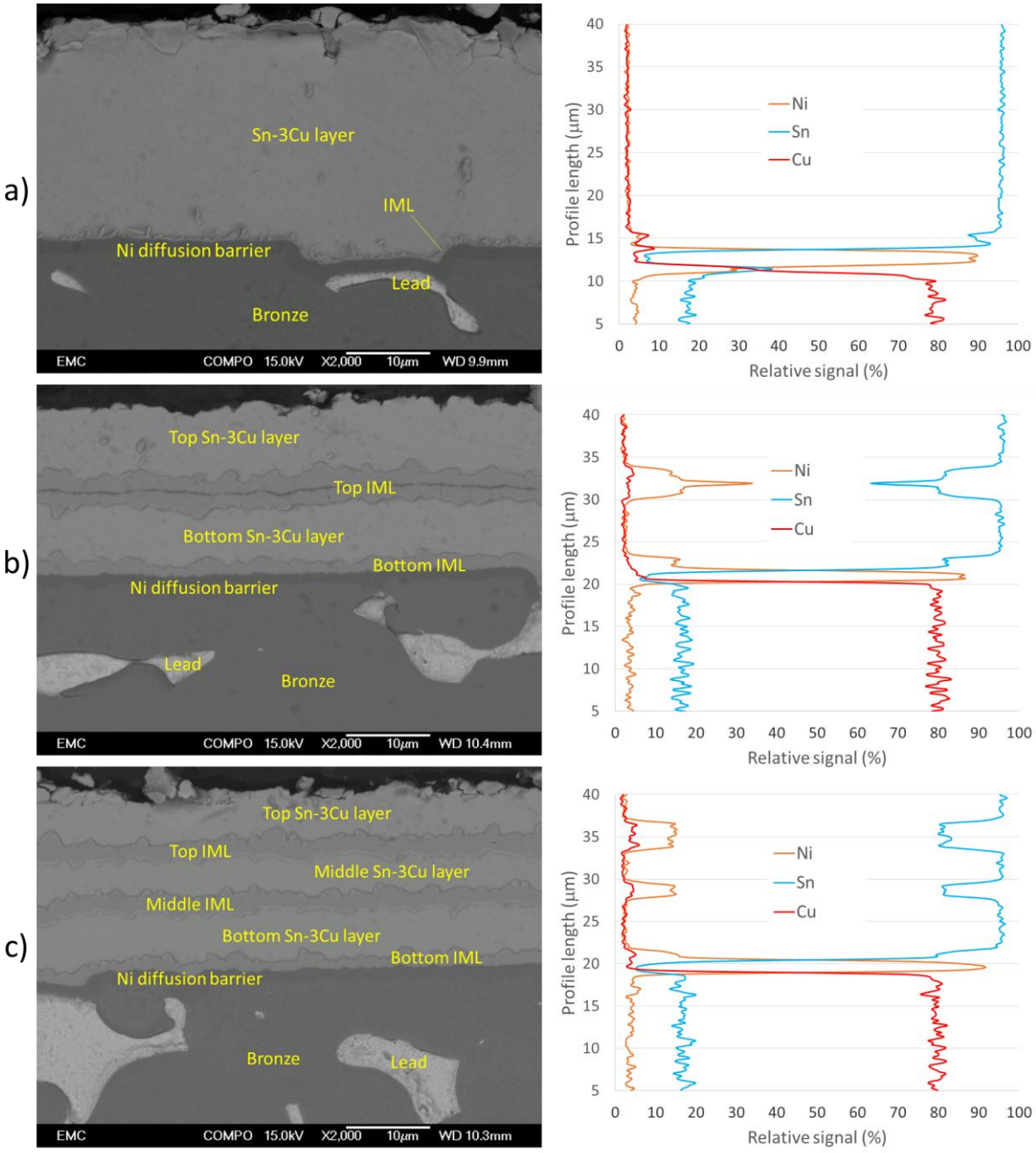

Figure 4. Backscatter image with compositional line scan for Ni, Sn and Cu in: a) 1IML, b) 2IML and c) 3IML coatings.

3.2 Application of lock-in thermography for crack detection

The objective of applying the thermography approach is to find a technique that can reliably detect the onset of cracking at an earlier stage than existing methods or criteria, (e.g. the compliance based failure criteria linked to a certain displacement under load control, discussed in section 3.3). This technique is also a non-contact and non-destructive technique, allowing extra information during the fatigue test to be obtained without introducing any potential damage to the samples, thus helping to gain understanding on how the cracks initiate and grow.

In order to apply lock-in thermography, samples under infra-red observation need to behave like a 'black body', i.e. only emitting heat radiation, in order to avoid reflections of radiation coming from surrounding bodies and external sources. In addition, this will maximize the measured response and

reduce signal to noise ratio. For this reason, the surface of samples are typically coated with a matt black paint to create a uniformly and high emissivity surface [36]. However, it is important that the correct thickness and type of coating is achieved. If the paint is too thin, the sample will not be opaque and will reflect radiation from other bodies (increasing noise); conversely, if the paint is too thick, the signal will suffer a delay or lag (since the paint acts as a thermal insulator, and its temperature lags that of the substrate beneath it [41, 42]). Therefore a study was required to determine the optimum paint thickness which was conducted in accordance with the procedure outlined in [43]. It was concluded that ~21 μm was the optimum thickness since the thermoelastic signal was maximised while being independent of loading frequency.

A further study was conducted to correlate between cracks detected using the infra-red detector and those seen under the optical microscope in order to confirm that the phase changes observed in the infra-red images are caused by the appearance of cracks, as detailed in section 2.5. Three bearings with 1IML were tested with a load amplitude of 315 N, at 10 Hz and a load ratio of 0.1, whilst being recorded with the infrared detector at 500 cycle intervals. The first bearing was tested for a total of 5000 cycles, and the test was stopped every 1000 cycles to observe the coating surface under the optical microscope. The second bearing was tested for 10000 cycles in total and stopped only once at 5000 cycles, and the third was tested for 20000 cycles in total and stopped only once at 10000 cycles. After the tests, the images obtained using the optical microscope and the infra-red camera were compared qualitatively. Figure 5 shows the comparison of images for the first tested bearing, where it can be seen that after 3000 cycles, damage is found at the same position with both techniques. It is noteworthy that we found similar results with the second and third bearings, confirming these results. Therefore, a qualitative correlation between cracks observed using optical microscope and the phase changes obtained in the infra-red images exists. Thus confirming that the change in phase on the surface of the sample is indicating the presence of cracks and identifying their location.

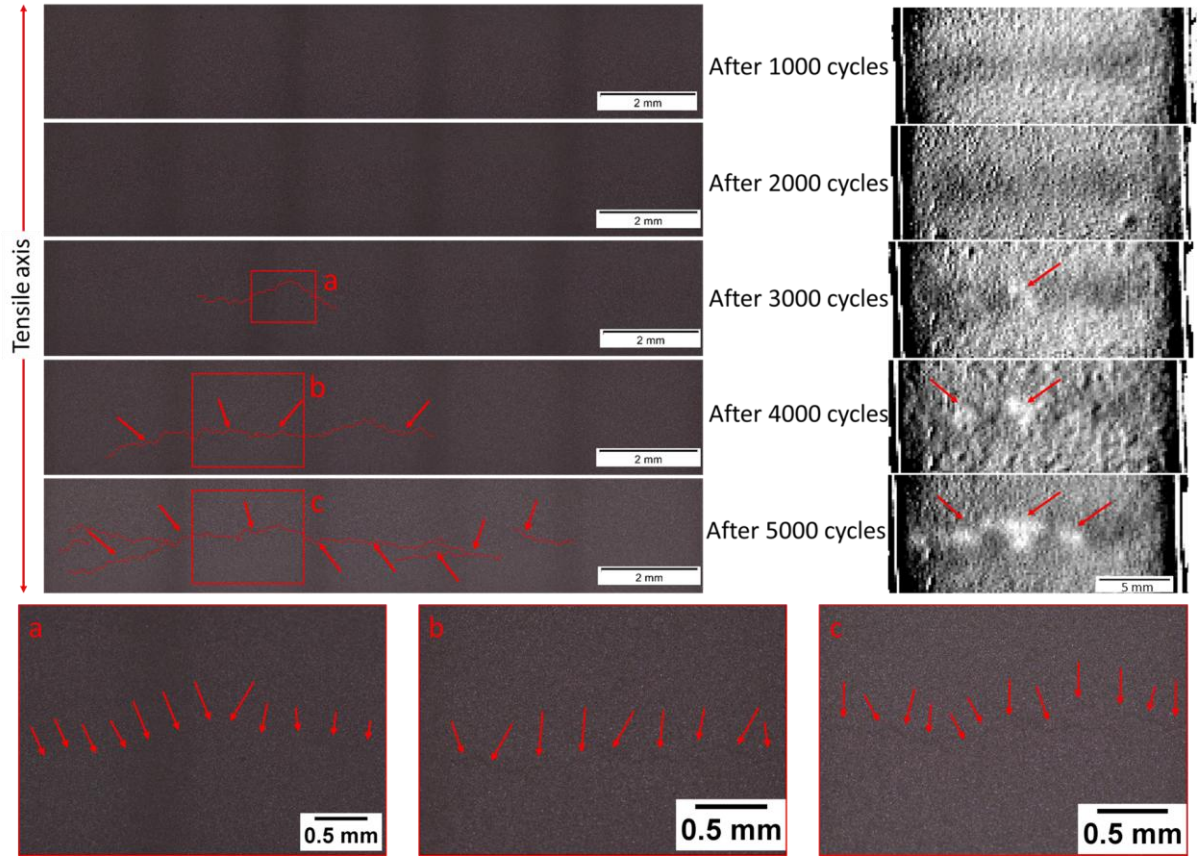

Figure 5. Comparison between images taken with an optical microscope and phase images taken with an infra-red camera (the red arrows point at cracks in the micrographs and sudden phase change in the phase images).

3.3 Fatigue tests

The fatigue tests were intended to assess the fundamental fatigue behaviour of these multilayer materials architectures. Hence, the tests do not aim to simulate the complex stress and strain conditions which a bearing in service will suffer due to the rotation of the journal against it. Instead, tests were conducted under 3-point bend, simplifying the load states and the conditions in order to have more control of the factors that could affect fatigue. Using this configuration, the maximum stress developed in the overlay is in a line below the top roller load application, ensuring localization of (and hence easier study of) the cracks.

In Figure 6 the results of fatigue tests for 30 bearings (3 coatings, 5 load conditions and 2 repetitions, all with the same dimensions) are plotted using a compliance based failure criterion. This criterion was used in order to ensure that the tests were terminated when all the bearings had reached a similar degree of fatigue damage, and to determine the number of cycles to a certain level of failure. While running the test, the displacement of the sample was monitored; failure of the sample was deemed to occur when the minimum position of the load cell had displaced by 0.1 mm from the initial minimum value. At this point the sample coating presents a substantial amount of surface cracks but without gross failure of the bearings occurring. In the first few loading cycles the minimum position tends to change significantly due to the sample settling in the rig, thus the initial displacement value was defined as the displacement after 1000 cycles.

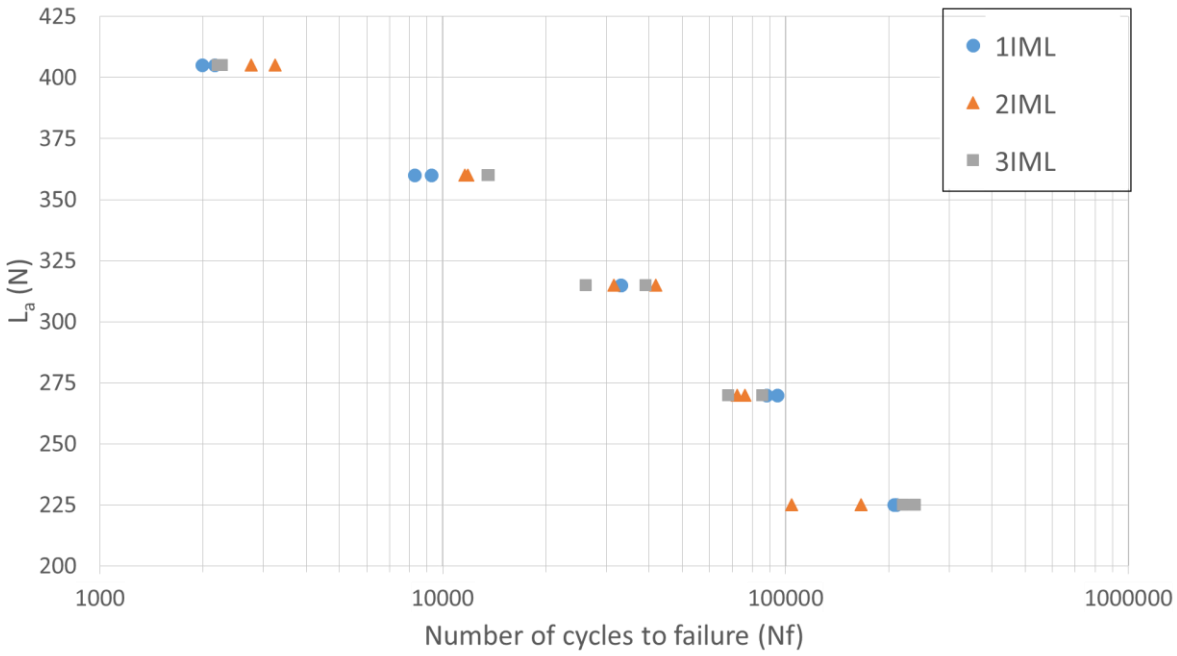

Figure 6. L_a-N curve, plotting the load amplitude versus the number of cycles to failure using the compliance failure criterion for 1IML, 2IML and 3IML.

From these results one may observe that there is not much difference in the performance of the tested bearings in terms of their lifetimes as a function of applied load, since the scatter in the results within a particular bearing class is sometimes greater than the difference between classes. This can be considered in terms of the crudeness of the chosen failure criterion, which accounts for the compliance of the whole sample, which is mostly the steel backing. This criterion assesses then mainly the response of the steel backing, which is the essentially the same for all the bearings. By sectioning some of the bearings, we found that in all of them the fatigue crack had penetrated into the steel at the point when the tests were stopped on achieving the compliance change criterion. Thus confirming the lack of sensitivity in assessing particularly the fatigue response differences in the thin overlay coatings, which is of far greater interest for the service failure assessment. This motivated our move to use another failure criterion based instead on the surface damage detection made possible by infra-red thermography.

The use of thermography provides a wealth of data around the zone of maximum stress/strain, enabling full-field information about crack evolution to be obtained. Use of such a technique in-situ helps to provide valuable information about the crack initiation and crack growth on the surface of the coating, and to set a more sensitive failure criterion based on these crack-related features. Therefore fatigue tests were conducted while recording data with the infra-red camera, and the obtained phase images were subsequently processed to obtain binary images at the different stages of testing in order to detect crack evolution on the surface of the coating during the fatigue tests. This information can then be used to establish a failure criterion that is far less conservative (and explicitly linked to the very early stages of crack initiation and growth in the multilayer overlay coatings) than the more gross failure criterion based on the compliance of the sample. This then will allow ranking of the coatings in terms of fatigue processes occurring principally in the overlay coatings (which has much higher service relevance). The criterion used was defined as the earliest image that could detect cracks reliably on the infra-red data recorded throughout the test. Based on the study described in section 3.2, the minimum crack length that could be detected was around 0.7 mm, so this was defined as the damage initiation detection limit and the corresponding lifetimes

were identified. In Figure 7 one can see the results for 34 bearings, where we can discern the different fatigue performance of the three coatings in terms now of the new lifetime observed as a function of the load amplitude (all bearings had the same overall dimensions to within a tolerance of 0.02 mm). Figure 7 shows now a clear separation of the best performance of 2IML and the worst performance for 3IML indicating that this method has a higher sensitivity for detecting initiation of damage and evaluating different coating systems under this simplified fatigue loading. They also show a lower scatter in the results with respect to Figure 6, indicating the better consistency of such a determination of lifetime to a similar level of damage initiation (~0.7mm surface crack length). Some of these tests were then stopped as soon as damage was detected (~0.7mm surface cracks), with the objective of studying in detail some of the shorter cracks. Looking at these smaller cracks at high resolution provides insight into the processes occurring during crack initiation and early crack propagation within these multilayer coatings to elucidate the reasons why the 2IML coating architecture is performing better than the 3IML system. It is noteworthy that any tests above a load amplitude of 315 N conducted with the infra-red camera, detected damage at these higher loads in the very first cycles, so the lifetime to early crack formation was effectively zero in these cases and has not been plotted in Figure 7.

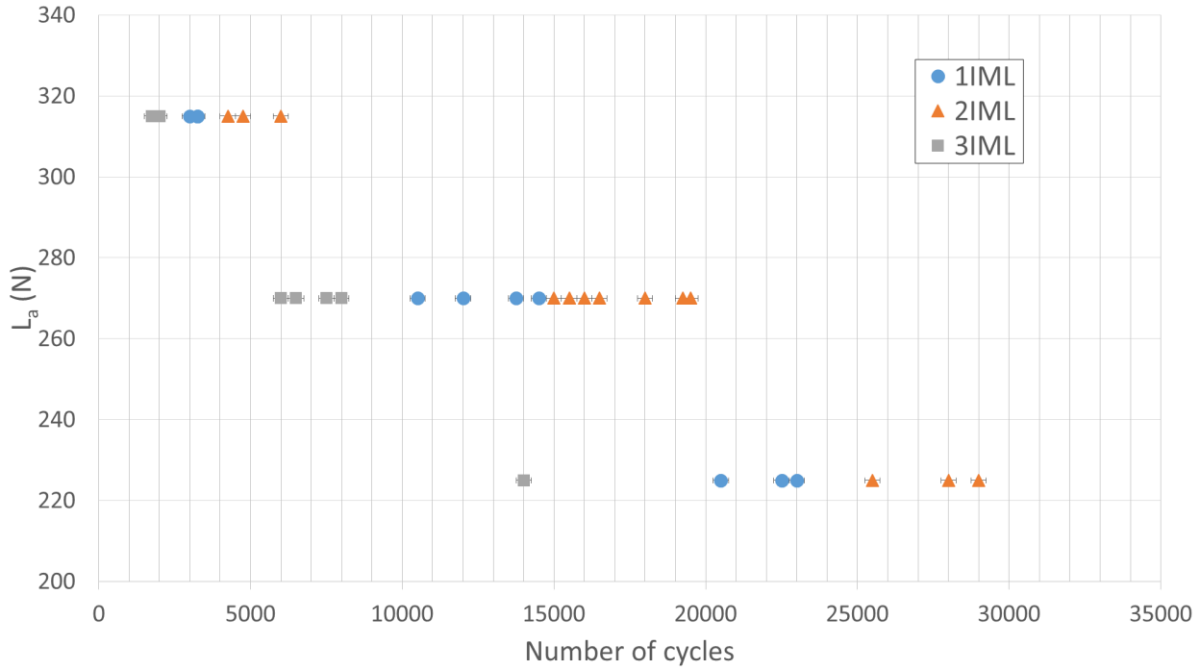

Figure 7. L_a-N curve, plotting the load amplitude versus the number of cycles to damage detection using lock-in thermography for 1IML, 2IML and 3IML.

The lifetimes obtained applying the lock-in thermography approach are linked to much earlier stages of damage and so are much shorter than the life-time obtained using the grosser compliance based failure criterion (where the crack had propagated into the steel backing). In Figure 8 we can see that by using the new damage initiation methodology (cracks ~0.7mm), the lifetime occurs between 5-25% of the lifetime obtained with the old methodology (i.e. the point of crack growth into the steel backing, the gross compliance criterion). Thus, this new methodology has established a failure criterion which is far less conservative than the previous methodology and has more direct service relevance to the failure processes of the overlay coating.

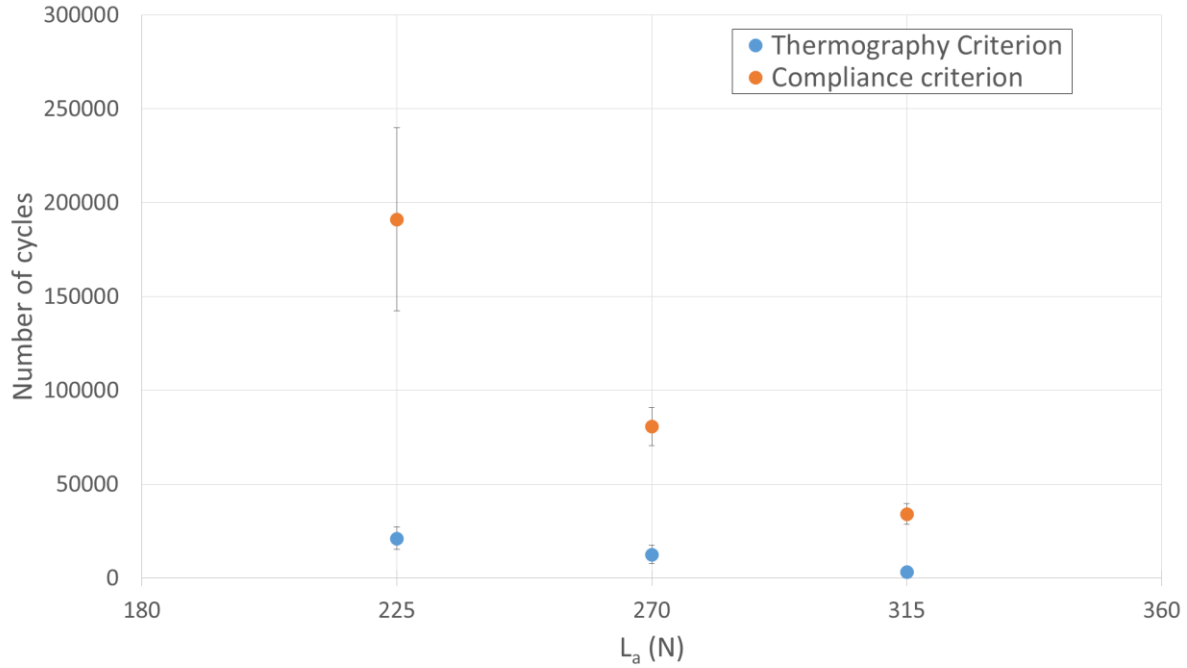

Figure 8. Failure criteria comparison between the compliance criterion and the thermography failure criterion in terms of number of cycle to damage detection versus load amplitude (L_a).

Strain gauges were placed on the coatings to evaluate the strain level developed on the overlay coating surface at the applied loads during these accelerated fatigue tests. We then emulated the load conditions of an accelerated test whilst measuring the evolving strain in the overlay coating surface. We used two frequencies during the test: first we ran the tests at 10 cycles per second until the strain stabilized, since during the first few cycles we observed significant work-hardening, and then slowed down the test frequency to 1 cycle per second in order to record the stabilised cyclic stress-strain in detail and to allow accurate measurement of the total strain range. We confirmed that there is no strain rate effect on the measured stresses and strains between these 2 frequencies. We carried out these cyclic tests for all three overlays, using the five load conditions used for the accelerated fatigue tests, and focussed on characterising the cyclically stabilised strain range, since we observed strain ratcheting during the test. The results are shown in Figure 9, where we can observe that the strain range increases with the load applied. From this plot it can be seen that 1IML is the coating that presents the highest amount of deformation under these load controlled tests. This can be attributed to the strength contribution of the aligned hard intermetallic layers, which can be expressed by a simple rule-of-mixtures approximation along the applied stress direction:

$$\mathrm{E_c} = \mathrm{E_{Intermetallic}X_{Intermetallic}} + \mathrm{E_{Sn}X_{Sn}} \qquad \textit{Equation 1}$$

$$\sigma_{\mathrm{yc}} = \sigma_{\mathrm{yIntermetallic}}\mathrm{X_{Intermetallic}} + \sigma_{\mathrm{ySn}}\mathrm{X_{Sn}} \qquad \textit{Equation 2}$$

Where E_C and σ_{yc} are the moduli and the yield strength of the coating, $E_{Intermetallic}$ and E_{Sn} are the moduli of the intermetallic material and Sn layer, respectively, and $\sigma_{Intermetallic}$ and σ_{Sn} are the yield strength for the intermetallic material and Sn layer; and $X_{Intermetallic}$ and X_{Sn} are the volume fractions of the intermetallic compounds and Sn phases in the coating. Therefore, the Young's modulus and the yield strength for 1IML are expected to be lower due to the lesser amount of hard intermetallic in the coating structure. 1IML contains around 3% of hard intermetallic materials, whilst 2IML and 3IML contain around 25% out of the overall coating (calculated by area fraction analysis). Thus, the

average Young's modulus and yield strength would be higher for 2IML and 3IML, which means that the strain range would be reduced compared with 1IML. However, 3IML shows less deformation than 2IML with the same expected volume fraction of hard material. This could also be considered in terms of the Hall-Petch [44, 45] equation which can also be applied for multilayer materials (Equation 3) [46]:

$$\sigma_y = \sigma_0 + Kd^{-1/2} \qquad \textit{Equation 3}$$

Where σ_y is the yield stress of the material, σ_0 and K are material-dependent constants, and d, in multilayer materials, is the bilayer thickness of the component phases. In this case, the Hall–Petch relation is based on the pile-ups of a large number of dislocations at the interface of multilayers. Since d is smaller in 3IML (~7 μm), its yield stress is predicted to be higher than 2IML (~10 μm). In our case we would expect an increase of 20% in the yield strength of 3IML compared with 2IML. Therefore, the thinner the bilayer thickness, the higher predicted yield strength, reducing the strain range. This can be explained by the mobility of dislocations. The plastic deformation in thin layers becomes more difficult because dislocations have shorter mean glide distances due to the barrier effect of the interfaces in the multilayers. This is because the dislocations in soft Sn layers can pile-up at the interfaces, and cannot glide across these interfaces because of the lattice and elastic modulus mismatches. Hence, the plastic strain experienced by the coatings will decrease with decreasing layer thickness [46].

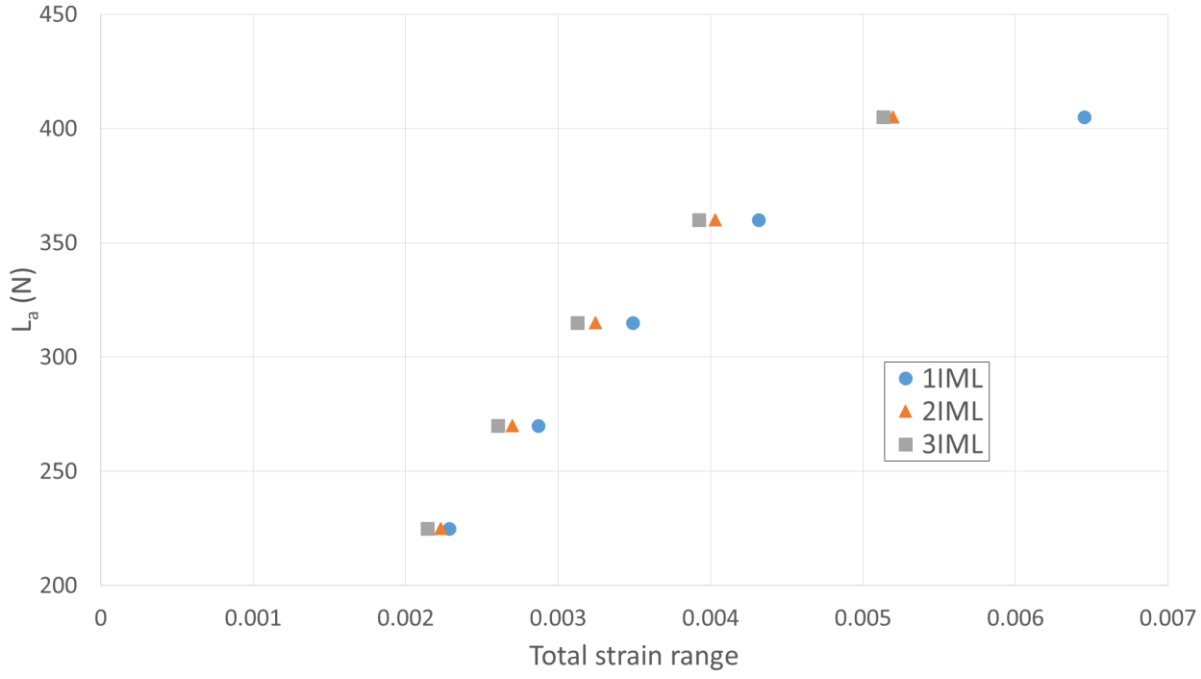

Figure 9. Total strain range for 1IML, 2IML and 3IML.

Although, we have used load amplitude versus number of cycles as a first approximation to compare the fatigue performance of different coatings, we can also combine Figure 6 and Figure 7 with Figure 9 in order to better rank such coatings by using the strains measured on the surface of the overlay coating during fatigue tests, which may better describe the behaviour developed in the coating during the fatigue tests. In Figure 10 one can see how by using the lock-in thermography technology, we can observe a more significant difference regarding the fatigue performance of the three

coatings considered in this study when the lifetime to damage initiation in the overlay coating is considered in terms of the total strain experienced in the overlay coating.

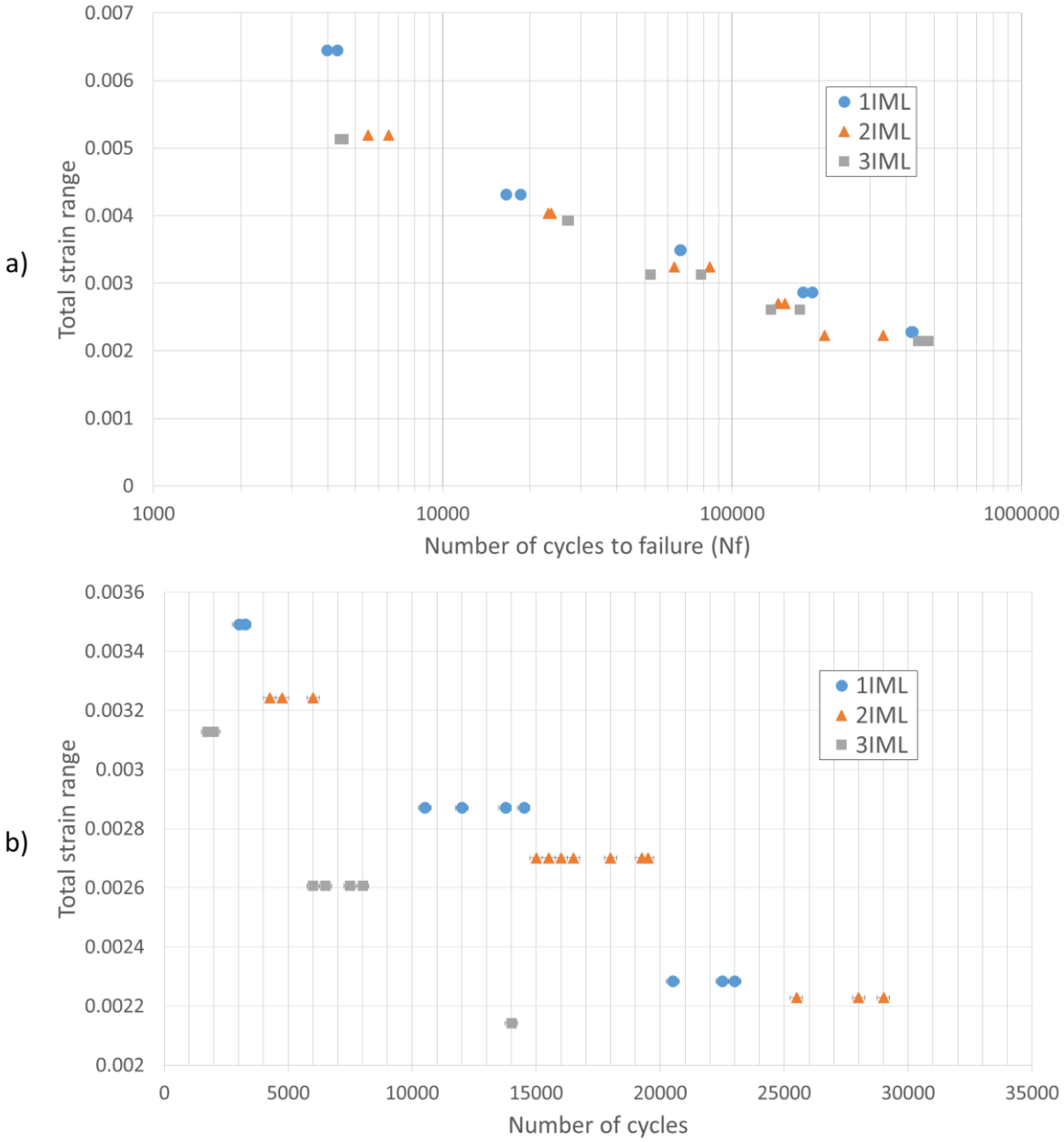

Figure 10. Δε-N curve, plotting the total strain range versus the number of cycles to failure using: a) compliance failure criterion and b) failure criterion by using lock-in thermography for 1IML, 2IML and 3IML.

3.4 Post-test observations

Thermographic observations

In addition to establishing a more service relevant failure criterion, the processed images taken with the infra-red camera can also be used to observe the evolution of damage during the fatigue tests. For example, in Figure 11 we can see the initiation and growth of cracks in 1IML, tested at L_a=315 N and N_f=32984 cycles (using the compliance failure criterion). In these images the damage, in white, grows along the 'x' axis (along the width of the sample), being the tensile axis perpendicular to the 'x' axis. In this case, we can see how the cracks initiate on the left side of the bearing, propagating

perpendicular to the tensile axis towards both edges. This allows assessment of the location of crack initiation and the evolution of crack propagation, facilitating any subsequent search for cracks at high or very high magnifications. Higher magnification observations will help to understand the failure mechanisms of these samples in particular, and by extension offers similar opportunities to other fatigue tests in other systems, highlighting the potential of this combination of methodologies.

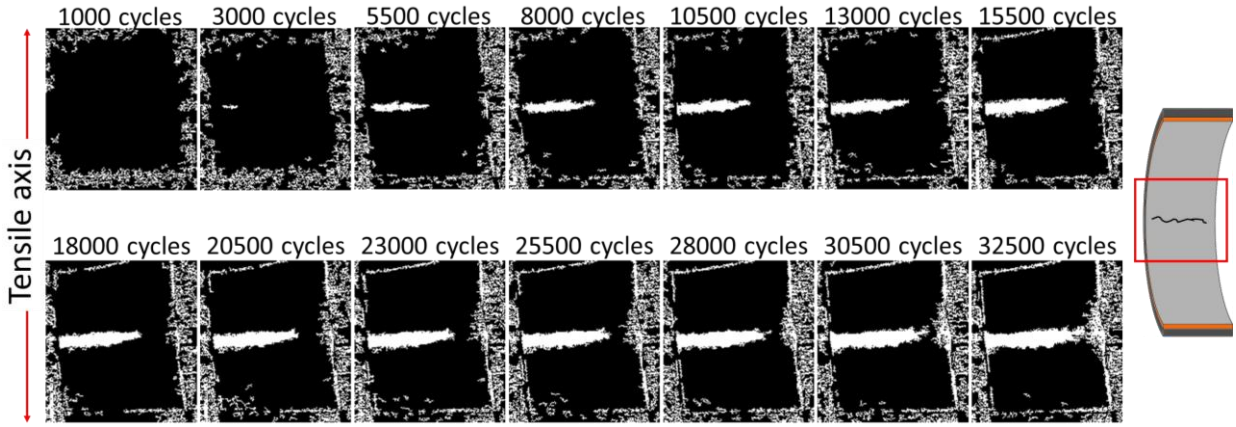

Figure 11. Post-processed infra-red images showing the evolution of damage in a 1IML tested at 315 N of load amplitude (total strain range = 0.003491).

Surface observations

After these accelerated fatigue tests, the bearings were also examined by optical microscopy in order to observe the amount of damage and crack morphology development from the top surface. In Figure 12 we can see surface crack observations for each of the coatings tested at 225 N of load amplitude (total strain range for 1IML, 2IML and 3IML are 0.002284, 0.002228 and 0.002142, respectively), for both cases stopping the fatigue tests using the compliance failure criterion (Figure 12a-c) and using the lock-in thermography as the failure criterion (Figure 12d-f). In the same set of images one can observe that different cracks have grown and coalesced together to form longer cracks, it is especially visible in Figure 12a-c, but also discernible in Figure 12g-i. It is also interesting to note that, although most of the cracks have propagated in the surface perpendicular to the tensile axis, some of the smaller cracks in Figure 12g-i appear to propagate at an angle to, or even parallel to, the tensile axis in order to coalesce as longer cracks, indicating the locally complex stress state in which the cracks are propagating. We can also see that the relatively high roughness of the electroplated surface is making any detailed observation (including grain size) difficult, since the surface cannot be mechanically polished without removing the very thin, soft Sn based overlay itself (which is the focus of the research investigation).

One can observe in the magnified images of the last three samples (Figure 12g-i) how different the crack fields are in the different coating architectures. In the 1IML architecture (Figure 12g) fewer cracks are observed but they appear thicker and longer, on the other hand, 3IML (Figure 12i) has more cracks but they are shorter and thinner, and finally, the 2IML architecture (Figure 12h) appears intermediate between the two previous cases. This could be linked to the strain range results at the same applied load if we consider that long cracks are also expected to be deeper [47], then it is evident that since 1IML experiences more total strain range for the same load, this may produce longer cracks, as the driving force for fatigue crack propagation will have been higher. It is less clear why the number of initiation sites may have varied between the architectures. Further consideration needs to be given as to why fewer longer cracks have given rise to a similar final failure displacement criterion (linked to significant crack penetration into the steel backing).

Also, from Figure 12g-i one can see that the surface paths of the cracks in 1IML seem to be more tortuous than those in 2IML and 3IML, and the cracks in 2IML more tortuous than the cracks in 3IML. This could be explained by considering:

1. Tin has a low melting point (231 °C), thus, the annealing temperature is sufficient for the Sn grains to grow in a columnar fashion in the deposition direction after the initial plating process (columnar grains of Sn can be seen in the cross-sections in Figure 13). Thus, structures with a thicker Sn layer are expected to allow larger Sn grains to grow (as can be seen in the cross-sectional images in Figure 13, where thicker Sn layers contain larger columnar Sn grains). Although we don't have direct observations of the grain size in the top surface plane, it is reasonable to expect that, the thicker the top-surface Sn layer, the coarser the grain size in the Sn.

2. The fatigue cracks at room temperature usually propagate along tin grain boundaries (examples of intergranular crack propagation can be seen in the overlay cross-sections in Figure 13). As the fatigue tests are conducted at room temperature (~21 °C), which is 58% of the absolute melting point for pure Sn, these then can be considered as effectively high temperature or time-dependent fatigue tests [48]. This creep-fatigue regime would also explain the ratcheting strain performance seen under cyclic loading and the possible effects of creep fatigue need to be considered. Typically intergranular crack growth is seen under creep-fatigue conditions.

Thus, it is possible that, the thicker the final top-surface Sn layer in the overlay, the larger the expected columnar grain size and so the more tortuous the surface cracks would be, if they are indeed growing intergranularly. This increase in tortuosity with Sn layer thickness is indeed seen in Figure 12g-i. This would also explain some of the differences in the observed crack field distributions between the coatings. A thinner Sn coating being expected to have a smaller grain size and more grain boundaries, and hence more potential crack propagation routes, perhaps creating the higher density of cracks (although the initiation process at a microstructural level still needs to be confirmed). As a result, it is likely that a coarser grain size in the thicker Sn coatings will have a better fatigue performance, since intergranular fatigue processes will be expected to pre-dominate and will be less prevalent with a coarser grain size. Thus, a Sn microstructure with bigger grains will have a higher creep resistance [49] offering less crack propagation paths and these will also be more deflected (and so offer additional intrinsic and extrinsic shielding effects to crack propagation rates). These additional factors may explain why 1IML has a better performance than 3IML, since the latter is composed of thinner Sn layers, hence, potentially a smaller Sn grain size and worse creep-fatigue resistance.

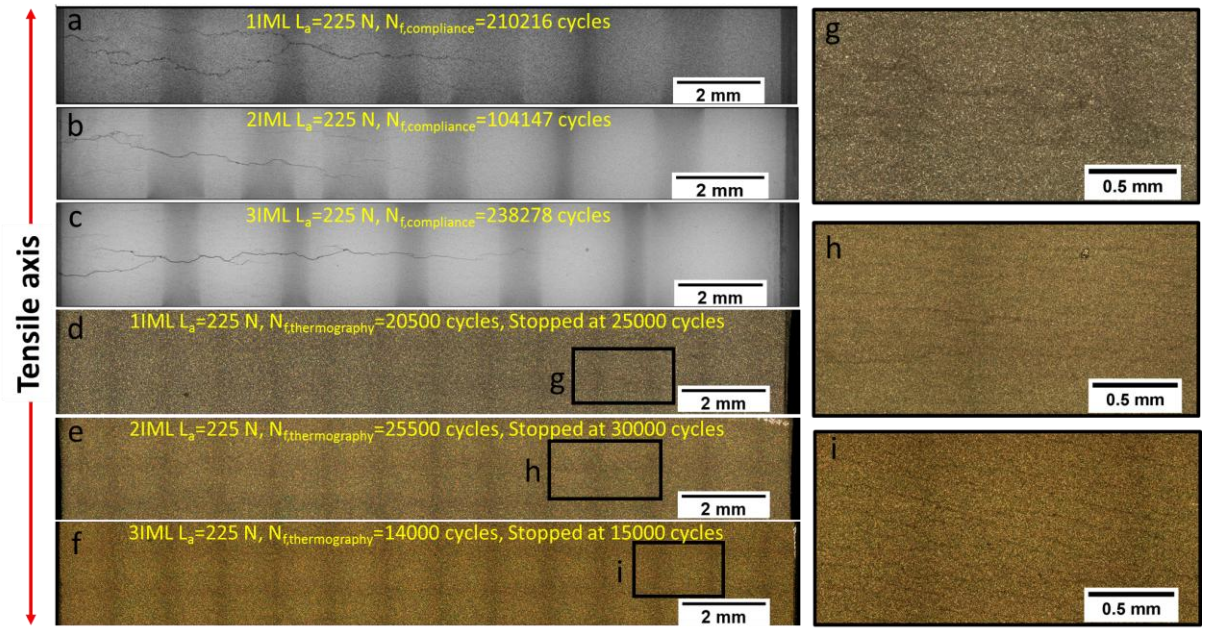

Figure 12. Surface cracks on six samples (two for each type of coating) tested under the same conditions, the three top stopped using the compliance failure criterion and the other three using lock-in thermography.

Cross-sectional observations

Examples of intergranular crack propagation in Sn can be seen in Figure 13, where we have used FIB to obtain cross-sections of some of the fatigue cracks seen on the bearing overlay surface. Firstly, one can see in Figure 13a a fatigue crack in 1IML, which propagates along the columnar tin grain boundaries towards the intermetallic layer, where it seems to be arrested. Due to this phenomenon the crack path was observed to present a higher degree of tortuosity in the Sn layers than in the intermetallic layers. Secondly, in Figure 13b we can see cracks in 2IML with some degree of deflection in the interface between the Sn layer and the intermetallic layer, where the crack changes its direction following the interface until it eventually penetrates to the harder material. It is noteworthy that in most of the observations the cracks are deflected and sometimes arrested in the Sn layers in between the intermetallic layers. Thirdly, in Figure 13c we can observe the crack path in 3IML, which also presents some degree of deflection, where the cracks propagate along the tin-intermetallic interface. Finally, we have also observed in some cases that the cracks initiate on the top surface, usually from stress-raisers induced by surface roughness that are found between Sn grains. Moreover, in all three architectures the direction of the crack propagation in Sn-Ni intermetallic and pure Ni layers is mostly perpendicular to the tensile axis, however in the Sn based layers the angle of propagation changes frequently as it follows the grain boundaries.

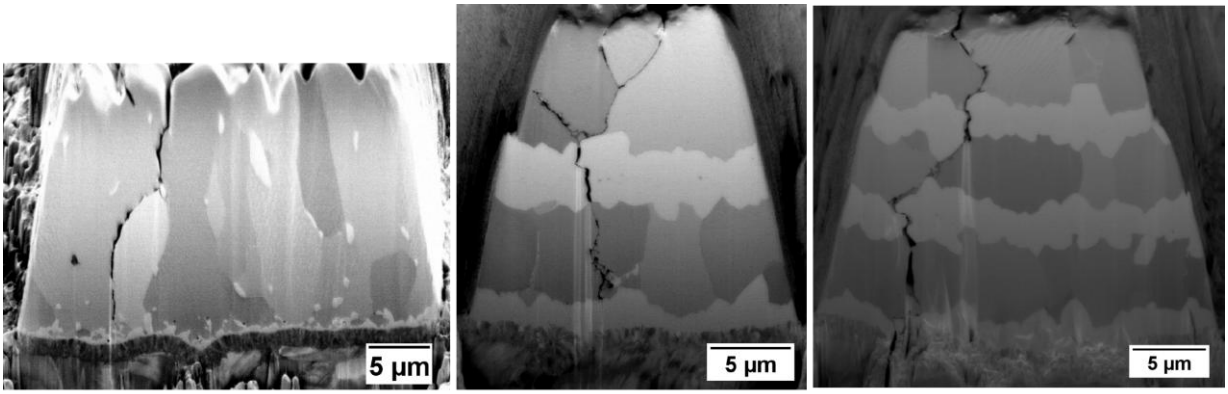

Figure 13. Cross-sectional image of cracks growing through the multilayer coatings: a) 1IML La=225 N, $N_{f,thermography}$=20500 cycles, Stopped at 25000 cycles; b) 2IML L_a=225 N, $N_{f,thermography}$=25500 cycles, Stopped at 30000 cycles; c) 3IML L_a=225 N, $N_{f,thermography}$=14000 cycles, Stopped at 15000 cycles.

Multilayer materials exhibit different fatigue crack growth behaviour than monolithic materials. This is attributed to the behaviour of a fatigue crack as it approaches a bi-material interface. *Suresh et al.* [50, 51] observed that a fatigue crack propagating normally to the interface from the harder side, would pass through the interface un-deflected, whereas a crack propagating from the softer side exhibited reduced crack growth rate, crack deflection and arrest. *Sugimura et al.* [52] found that a crack approaching the interface from the softer side experienced a significant drop in driving force as it approached the interface; it is this shielding effect that causes the experimentally observed reduction in fatigue crack growth rates. On the other hand when a crack grew from the harder material, anti-shielding effects would cause an increase of the crack growth rates when approaching the interface. Thus it was demonstrated that an interface between two plastically dissimilar materials had the potential to severely affect the propagation behaviour of an approaching fatigue crack. Moreover, Joyce et al. [53] showed the effect of layer thickness on the driving force of fatigue cracks growing from an effectively softer material, showing a decrease of the shielding effect when decreasing the thickness of the harder material. This was attributed to the thinner hard layer producing a smaller region of raised local stiffness within the adjacent soft layer.

Unlike the other structures, in 1IML deflected cracks were not typically observed along the interface between layers, this may be due to the thickness of the hard layer, as in this case the intermetallic layer is much thinner than in the other coating structures. As already mentioned, thicker hard layers may increase any shielding effect as a crack tip advances. Moreover, the deflected, bifurcated and arrested cracks found in 2IML and 3IML are thought to result from the succession of shielding effects performed by the varying intermetallic layers, due to the significant expected change of mechanical properties between Sn and Sn-Ni intermetallic compounds, effectively meaning the crack is propagating through soft->hard->soft layers and so on. Although examples of crack arrest were found in both 2IML and 3IML, they were more apparent/frequent in 2IML, which may explain the difference in lifetime observed between the tested samples.

This preliminary set of observations would appear to indicate that the soft-hard-soft overlay structure is more beneficial in providing significant crack deflection than the soft-hard-soft-hard-soft overlay structure. The direct link to fatigue resistance however needs to be carefully evaluated in light of the evolving strain conditions in the different overlays. Establishing which factor is affecting the crack-path and what the benefit might be to overlay fatigue performance in optimising such deflection will be a focus for future study.

4. Conclusions

In summary, a new methodology combining a number of techniques has been established to assess the fatigue performance of multilayer coatings. This methodology is able to consistently detect damage in the overlay coatings subjected to fatigue testing, hence, it is possible to rank different thin overlay coating structures in terms of their fatigue response. Moreover, the approach used has allowed us to locate the damage origin and observe the evolution of such damage during the tests, using non contacting full-field techniques, without test interruption. The use of the lock-in thermography establishes a failure criterion that is much less conservative than a failure criterion based on the compliance change of the sample, detecting damage much earlier. This eases study of the micromechanisms that control the fatigue performance of such multilayer coatings.

The fatigue tests revealed a better resistance to early damage in the coating with two hard layers (2IML) and the worst fatigue damage resistance was developed by the coating with three hard layers (3IML). It is proposed that the balance between several mechanisms may explain the different fatigue performance of the presented coatings:

- Less Sn or thinner Sn based layers which are more constrained by the IMC, make the system less compliant (decreasing the strain range experienced) and more brittle. This can also be linked to the stress relaxation that Sn provides, hence, less Sn or more constraint of thinner Sn layers will allow less stress relaxation of the system.
- Higher surface roughness may cause higher stress concentration on the top Sn surface, leading to earlier crack initiation. Also, differences in the roughness of the IMC layers can create preferential sites for subsurface crack initiation or propagation.
- Different population, shape and size of defects between coatings might also affect their fatigue performance by creating sites of preferential initiation or propagation.
- Creep can also control propagation processes, since the fatigue tests were done at a high homologous temperature for Sn. Hence, the grain size will affect the creep resistance: coarser grains will present better creep-fatigue performance.
- Crack shielding and anti-shielding effects will also influence the crack propagation. Differences in the thickness and properties of the coating layers will reduce or increase the crack growth rate, deflecting and even arresting cracks.

Although these proposed mechanisms are based on preliminary observations, a more detailed quantitative investigation of these phenomena is forthcoming in a future publication. The aim of the current work is to report on the methodology advances using these combined experimental mechanics approaches and how these have further elucidated the mesoscopic fatigue performance of the presented multilayer coatings, allowing overlay coating design to be evaluated more mechanistically and to inform new overlay coating design approaches.

Acknowledgements

The authors would like to thank Dr. Daniel Bull at University of Southampton for his assistance with image processing, Grazina Burmistroviene and Guy Lowman for their assistance on sample preparation and manufacturing. This work was supported by the Engineering and Physical Sciences Research Council (EPSRC, EP/M50662X/1) and Daido Metal Co. Ltd.

The accompanying data presented in this paper can be found via the doi: https://doi.org/10.5258/SOTON/D0087

References

[1] N. Gyde, Fatigue Fractures in Babbitt Lined Journal Bearings, Technical University of Denmark., 1969.
[2] H. Tsuji, Y. Tomita, N. Kawakami, I. Kerr, J. Harrison, Development of a new tin based overlay for medium speed diesel engines, CIMAC Congress 2004, Kyoto, (2004).
[3] Y. Zhang, I. Tudela, M. Pal, I. Kerr, High Strength Tin-based Overlay for Medium and High Speed Diesel Engine Bearing Tribological Applications, Tribology International, (2015).
[4] Y. He, S.C. Wang, F. C. Walsh, W. S. Li, L. He, P.A.S. Reed., The monitoring of coating health by in situ luminescent layers, Royal Society of Chemistry, 5 (2015) 42965-42970.
[5] M. Anand, G. Burmistroviene, I. Tudela, R. Verbickas, G. Lowman, Y. Zhang, Tribological evaluation of soft metallic multilayer coatings for wear applications based on a multiple pass scratch test method, Wear, 388-389 (2017) 39-46.
[6] W.H. Wilson, A test machine for assessing the fatigue properties of impulsively loaded plain bearings, Proceedings of the Institution of Mechanical Engineers, 182 (1967) 129-131.
[7] U. Wiklund, P. Hedenqvist, S. Hogmark, Multilayer cracking resistance in bending, Surface and Coatings Technology, 97 (1997) 773-778.
[8] P.M. Ramsey, H.W. Chandler, T.F. Page, Bending tests to estimate the through-thickness strength and interfacial shear strength in coated systems, Thin Solid Films, 201 (1991) 81-89.
[9] G. Gille, K. Wetzig, Investigations on mechanical behaviour of brittle wear-resistant coatings I. Experimental results, Thin Solid Films, 110 (1983) 37-54.
[10] M.C. Mwanza, M.R. Joyce, K.K. Lee, S. Syngellakis, P.A.S. Reed, Microstructural characterisation of fatigue crack initiation in Al-based plain bearing alloys, International Journal of Fatigue, 25 (2003) 1135-1145.
[11] M.S. Ali, P.A.S. Reed, S. Syngellakis, Comparison of fatigue performance of HVOF spray coated and conventional roll bonded aluminium bearing alloys, Materials Science and Technology, 25 (2009) 575-581.
[12] M. R. Joyce, S. Syngellakis, P.A.S. Reed, Fatigue crack initiation and early growth in a multiphase Al alloy included in a multilayer material system, Materials Science and Technology, 20 (2004).
[13] R. Jiang, S. Everitt, N. Gao, K. Soady, J.W. Brooks, P.A.S. Reed, Influence of oxidation on fatigue crack initiation and propagation in turbine disc alloy N18, International Journal of Fatigue, 75 (2015) 89-99.
[14] R. Jiang, N. Karpasitis, N. Gao, P.A.S. Reed, Effects of microstructures on fatigue crack initiation and short crack propagation at room temperature in an advanced disc superalloy, Materials Science and Engineering: A, 641 (2015) 148-159.
[15] B.Y. He, K.A. Soady, B.G. Mellor, G. Harrison, P.A.S. Reed, Fatigue crack growth behaviour in the LCF regime in a shot peened steam turbine blade material, International Journal of Fatigue, 82 (2016) 280-291.
[16] T. O. Mbuya, Y. Gu, R. C. Thomson, P.A.S. Reed., Effect of intermetallic particles and grain boundaries on short fatigue crack growth behaviour in a cast Al–4Cu–3Ni–0.7Si piston alloy, Fatigue & Fracture of Engineering Materials & Structures, 40 (2017) 1428–1442.
[17] A.C. Melado, A.S. Nishikawa, H. Goldenstein, M.A. Giles, P.A.S. Reed, Effect of microstructure on fatigue behaviour of advanced high strength ductile cast iron produced by quenching and partitioning process, International Journal of Fatigue, 104 (2017) 397-407.
[18] R. Jiang, F. Pierron, S. Octaviani, P.A.S. Reed, Characterisation of strain localisation processes during fatigue crack initiation and early crack propagation by SEM-DIC in an advanced disc alloy, Materials Science and Engineering: A, 699 (2017) 128-144.
[19] A. Lanzutti, M. Pujatti, M. Magnan, F. Andreatta, H. Nurmi, A. Silvonen, E. Hlede, L. Fedrizzi, Uniaxial fatigue properties of closed die hot forged 42CrMo4 steel: Effect of flash and mechanical surface treatments, Materials & Design, 132 (2017) 324-336.
[20] L. Yan, J. Fan, In-situ SEM study of fatigue crack initiation and propagation behavior in 2524 aluminum alloy, Materials & Design, 110 (2016) 592-601.

[21] E. Grinzato, C. Bressan, S. Marinetti, P.G. Bison, C. Bonacina, Monitoring of the Scrovegni Chapel by IR thermography: Giotto at infrared, Infrared Physics & Technology, 43 (2002) 165-169.
[22] M.R. Clark, D.M. McCann, M.C. Forde, Application of infrared thermography to the non-destructive testing of concrete and masonry bridges, NDT & E International, 36 (2003) 265-275.
[23] C. Meola, Infrared thermography of masonry structures, Infrared Physics & Technology, 49 (2007) 228-233.
[24] C. Badulescu, M. Grédiac, H. Haddadi, J.D. Mathias, X. Balandraud, H.S. Tran, Applying the grid method and infrared thermography to investigate plastic deformation in aluminium multicrystal, Mechanics of Materials, 43 (2011) 36-53.
[25] M.P. Luong, Fatigue limit evaluation of metals using an infrared thermographic technique, Mechanics of Materials, 28 (1998) 155-163.
[26] M.L. Pastor, X. Balandraud, M. Grédiac, J.L. Robert, Applying infrared thermography to study the heating of 2024-T3 aluminium specimens under fatigue loading, Infrared Physics & Technology, 51 (2008) 505-515.
[27] H. Wang, L. Jiang, P.K. Liaw, C.R. Brooks, D.L. Klarstrom, Infrared temperature mapping of ULTIMET alloy during high-cycle fatigue tests, Metallurgical and Materials Transactions A, 31 (2000) 1307-1310.
[28] H.X. Zhang, G.H. Wu, Z.F. Yan, S.F. Guo, P.D. Chen, W.X. Wang, An experimental analysis of fatigue behavior of AZ31B magnesium alloy welded joint based on infrared thermography, Materials & Design, 55 (2014) 785-791.
[29] X. Tong, X. Chen, J. Xu, C. Sun, W. Liang, Excitation of thermal dissipation of solid propellants during the fatigue process, Materials & Design, 128 (2017) 47-55.
[30] T. Ummenhofer, J. Medgenberg, On the use of infrared thermography for the analysis of fatigue damage processes in welded joints, International Journal of Fatigue, 31 (2009) 130-137.
[31] G. Fargione, A. Geraci, G. La Rosa, A. Risitano, Rapid determination of the fatigue curve by the thermographic method, International Journal of Fatigue, 24 (2002) 11-19.
[32] F. Curà, G. Curti, R. Sesana, A new iteration method for the thermographic determination of fatigue limit in steels, International Journal of Fatigue, 27 (2005) 453-459.
[33] P. Jiang, X. Fan, Y. Sun, D. Li, B. Li, T. Wang, Competition mechanism of interfacial cracks in thermal barrier coating system, Materials & Design, 132 (2017) 559-566.
[34] K. Gopinath, R.K. Gupta, J.K. Sahu, P.K. Ray, R.N. Ghosh, Designing P92 grade martensitic steel header pipes against creep–fatigue interaction loading condition: Damage micromechanisms, Materials & Design, 86 (2015) 411-420.
[35] Y. Zhang, E. Banchelli, M. Pal, I. Kerr, Lead-free tin based multilayer overlay for plain bearing, UK.
[36] M.H. Belgen, Infrared radiometric stress instrumentation application range study, NASA, 142 (1967).
[37] J. Chicken, Private communication with manufacturer, FLIR, (2010).
[38] J.M. Dulieu-Barton, P. Stanley, Development and applications of thermoelastic stress analysis, The Journal of Strain Analysis for Engineering Design, 33 (1998) 93-104.
[39] C.E. Ho, S.C. Yang, C.R. Kao, Interfacial reaction issues for lead-free electronic solders, Journal of Materials Science: Materials in Electronics, 18 (2007) 155-174.
[40] J.A.v. Beek, S.A. Stolk, F.J.J.v. Loo, Multiphase diffusion in the systems Fe-Sn and Si-Sn, Zeitschrift fuer Metallkunde, 73 (1982) 439-444.
[41] A.F. Robinson, J.M. Dulieu-Barton, S. Quinn, R.L. Burguete, Paint coating characterization for thermoelastic stress analysis of metallic materials, Measurement Science and Technology, 21 (2010).
[42] J. McKelvie, Consideration Of The Surface Temperature Response To Cyclic Thermoelastic Heat Generation, 1987, pp. 44-55.
[43] A.F. Robinson, Assessment of Residual Stress using Thermoelastic Stress Analysis, University of Southampton, 2011.
[44] N.J. Petch, The cleavage of polycrystals, Journal of the iron and steel Institute, 174 (1953) 8.

[45] E.O. Hall, The Deformation and Ageing of Mild Steel: III Discussion of Results, Proceedings of the Physical Society. Section B, 64 (1951) 747.
[46] W. Wang, R.N. Singh, Influence of the microstructure on the mechanical properties of Ni/Sn multilayered composites, Materials Science and Engineering: A, 271 (1999) 306-314.
[47] S.-X. Wu, Shape change of surface crack during fatigue growth, Engineering Fracture Mechanics, 22 (1985) 897-913.
[48] W. Wang, R.N. Singh, Fatigue crack growth in a Ni–Sn multilayered composite, Materials Science and Engineering: A, 251 (1998) 184-191.
[49] H. Abdel-Raouf, T.H. Topper, A. Plumtree, Fatigue At Elevated Temperatures, ASTM Special Technical Publication 1972.
[50] S. Suresh, Y. Sugimura, E.K. Tschegg, The growth of a fatigue crack approaching a perpendicularly-oriented, bimaterial interface, Scripta Metallurgica et Materialia, 27 (1992) 1189-1194.
[51] S. Suresh, Y. Sugimura, T. Ogawa, Fatigue cracking in materials with brittle surface coatings, Scripta Metallurgica et Materialia, 29 (1993) 237-242.
[52] Y. Sugimura, P.G. Lim, C.F. Shih, S. Suresh, Fracture normal to a bimaterial interface: Effects of plasticity on crack-tip shielding and amplification, Acta Metallurgica et Materialia, 43 (1995) 1157-1169.
[53] M.R. Joyce, P.A.S. Reed, S. Syngellakis, Numerical modelling of crack shielding and deflection in a multilayer material system, Materials Science and Engineering: A, 342 (2003) 11-22.

Data Statement

Click here to download Data Statement: dataprofile.xml